An Investigation of the Impact of Canadian wildfires on US Air Quality using Model, Satellite and Ground Measurements

Zhixin Xue[1*], Nair Udaysankar[2], and Sundar A. Christopher[2]

[1]Department of Chemical and Biochemical Engineering, The University of Iowa, Iowa City, IA, USA.
[2]Department of Atmospheric and Earth Science, University of Alabama in Huntsville, Alabama, USA.
[*]Corresponding author. Email: zhixin-xue@uiowa.edu

Abstract.

Canadian wildfires transport large concentrations of particulate matter into the United States, leading to various impacts on surface temperature, radiation balance, visibility, and exacerbating pollution-related respiratory conditions. Using a combination of surface, satellite and numerical models, this study quantifies the increase in surface fine particulate matter (PM2.5) in the Continental United States due to long-range transported smoke from Canadian wildfires during a wildfire episode from August 9th to 25th, 2018. As a widely used indicator of surface pollution levels, satellite-retrieved AOD can provide crucial information on columnar pollution mass. However, the daily spatial coverage of satellite AOD is restricted due to cloud cover. In order to quantify the daily changes of surface pollution, we fill in the AOD gaps by utilizing simulated 10-km spatial resolution AOD from a chemistry transport model (CTM). Meteorological variables influencing smoke transport were also integrated alongside the gap-filled AOD product to estimate surface PM2.5 using geographically weighted regression (GWR) and random forest (RF) models. The model with better performance was subsequently applied to quantify PM2.5 changes due to Canadian wildfires. To isolate the impact of Canadian wildfires, we calculate the surface PM2.5 ratio with and without Canadian fire sources by conducting two CTM simulations: one with Canadian wildfire emissions enabled and another with these emissions turned off. Our results show that Canadian wildfires caused a significant increase in surface PM2.5, contributing up to 28 μgm^{-3} (a 69% increase) across different US EPA regions during the August 2018 wildfire event.

1 Introduction

Airborne fine particulate matter (PM2.5), with aerodynamic diameters less than 2.5μm, is a well-documented contributor to increased mortality from diseases such as ischemic heart disease, chronic obstructive pulmonary disease, cardiovascular disease, respiratory disease, lung cancer, chronic kidney disease, hypertension, and dementia (Chen and Hoek, 2020; Bu et al., 2021; Bowe et al., 2019). In 2017, PM2.5 exposure was linked to 4.58 million deaths globally, with ambient PM2.5 accounting for 64.2% of these deaths (Bu et al., 2021). PM2.5 originates from diverse sources, including combustion processes, power plants, dust, sea salt, and secondary chemical reactions. In the United States, wildfires are a significant and growing source of PM2.5 pollution (O'Dell et al., 2019). For regions affected the most by wildfires, like the state of Washington (WA), an increase in daily PM2.5 of 97.1 μgm^{-3} during the summer of 2020 was found, which related to 92 more mortality cases

25 (Liu et al., 2021). Moreover, the toxicity of PM originating from wildfire smoke has been found to be 3-4 times greater than equivalent doses of ambient PM (Wegesser et al., 2009). Health impacts vary with chemical composition, which depends on biomass combustion stages and temperature (Kim et al., 2018; Aguilera et al., 2021). Beyond its health impacts, wildfire-related PM2.5 imposes considerable economic burdens. From simulation results, wildfire-related economic costs have been projected to increase from $ 7 billion per year to $ 43 billion per year in 2090 (Neumann et al., 2021).

30 Given the growing role of wildfires as a major PM2.5 source, accurately assessing pollution levels requires understanding the transport dynamics and chemical transformations of wildfire smoke, which are influenced by factors such as fire intensity, injection height, atmospheric dynamics, and terrain interactions. Higher fire radiative power (FRP) results in longer distances of the smoke transport due to higher plume injection heights (Solomos et al., 2015). A global analysis of over 23,000 wildfires found that significant injection heights into the free troposphere are primarily observed in the boreal forests of North America

35 and Siberia during the northern summer (Val Martin et al., 2018). Smoke remnants from Canadian stand-replacing forest fires have been observed at altitudes exceeding 13 km (Damoah et al., 2006). Once injected, smoke plumes can descend to the surface through a combination of subsidence, interception, and diurnal entrainment within the Planetary Boundary Layer (PBL), as observed in the Eastern US for 2002 July Canadian forest fire event (Colarco et al., 2004). Atmospheric circulation plays a key role in shaping smoke transport. Upper-level winds facilitate long-range horizontal transport, while surface high-pressure

40 systems enhance ground-level pollution through subsidence inversions (Miller et al., 2011). Cyclonic circulation can form a multilayer PBL, characterized by temperature inversions and stable stratification, which trap pollutants in convergent zones (Jiang et al., 2021b). Interactions with mountain terrain further modulate smoke dispersion: under stable synoptic conditions, valleys become more stagnant, while unstable conditions promote vertical mixing (Beaver et al., 2010; Lang et al., 2015). During transport, smoke particles undergo physical and chemical transformations that influence their sizes, such as hygroscopic

45 growth (Carrico et al., 2005; Gomez et al., 2018), SOA formation (Ahern et al., 2019), condensation of semi-volatile species (Reid et al., 2005; Zhou et al., 2017; Akagi et al., 2012), and coagulation process (Aloyan et al., 1997; Sun et al., 2019).

Estimating surface PM2.5 concentrations presents significant challenges due to spatial and temporal variability and limited ground station coverage. Traditional approaches, such as spatial interpolation (e.g., inverse distance weighting, ordinary kriging) rely primarily on ground-based PM2.5 measurements, while linear regression methods combine satellite-derived AOD

50 with surface PM2.5 measurements (Hoff and Christopher, 2009). More advanced methods, like multi-linear regression, typically incorporate surface PM2.5 data, satellite AOD, and meteorological datasets from models (Gupta and Christopher, 2009b). Geographically weighted regression (GWR) and machine learning methods use similar data sources as multi-linear regression but offer better spatial resolution and adaptability to local variations (Xue et al., 2021; Ma et al., 2014; Bai et al., 2016; Song et al., 2014; Hu et al., 2017; Gupta and Christopher, 2009a; Zamani Joharestani et al., 2019). Linear mixed-effect models add

55 temporal variability by including both fixed and random effects (Ma et al., 2016; Lee et al., 2011). While chemistry transport models (CTMs) leverage detailed atmospheric chemistry and physics simulations using emissions inventories, meteorological fields, and chemical species distributions (Geng et al., 2015; Xue et al., 2019). Traditional methods like spatial interpolation and linear regression struggle to integrate multiple mechanisms and spatial-temporal variables, a limitation newer techniques address (Zhang et al., 2018). Due to the growth of computing power, machine learning (or artificial intelligence) has become

a major focus for estimating the spatial-temporal dynamic distribution of surface PM2.5 concentrations (Zhang et al., 2018; Sayeed et al., 2022).

Satellite-retrieved AOD serves as a valuable indicator of columnar pollution, providing critical information for estimating surface PM2.5 concentrations, though it is not a direct measurement of surface pollution (Wang and Christopher, 2003; Geng et al., 2015). Its key advantages include over two decades of data availability from polar-orbiting sensors and the extensive spatial coverage of satellite observations, making it a powerful tool for long-term air quality analysis. However, cloud cover frequently obstructs AOD retrievals, limiting their utility for daily surface PM2.5 estimation (Goldberg et al., 2019). To overcome this limitation, gap-filling methods are used to generate spatially and temporally continuous AOD datasets. These methods include fusing retrievals from multiple satellite sensors (Ma et al., 2014), applying multiple imputation techniques using auxiliary data such as cloud fraction, elevation, and humidity (Xiao et al., 2017), and using statistical approaches like Kriging to interpolate AOD based on seasonal and regional AOD:PM2.5 ratios derived from ground-based measurements (Lv et al., 2017). Additionally, incorporating chemistry transport model (CTM) simulations into the gap-filling process has been shown to significantly improve the accuracy and reliability of imputed AOD values (Xiao et al., 2021). The AOD-PM2.5 relationship is influenced by aerosol composition, vertical distribution, and meteorological factors. Planetary Boundary Layer Height (BLH) serves as a key indicator by representing the mixing height of aerosols and their influence on surface pollution levels (Gupta and Christopher, 2009b). Surface pressure also plays a role, with high-pressure systems linked to surface pollution increases due to subsidence inversions (Miller et al., 2011). Additionally, Relative Humidity (RH) affects this relationship, as AOD is sensitive to particle size and hygroscopic growth (Li et al., 2014), while PM2.5 reflects dry mass. Incorporating these meteorological parameters helps models better capture the dynamic processes shaping the AOD-PM2.5 relationship.

This study is designed to assess the pollution change due to fine particulate matter in the United States transported by smoke from Canadian wildfires and to also examine the physical processes during transport that affects surface pollution along the path. First, by turning on and off the fire emissions in the CTM in Canada, we conduct two WRF-Chem simulations to investigate the processes that influence the transport of remote smoke aerosols in the atmosphere. According to the analysis of different processes, we then selected variables associated with smoke's vertical distribution, which determined the relationships between AOD and surface pollution concentrations. Finally, by filling in the satellite AOD gaps due to cloud covers using CTM simulations, we estimate the surface pollution increase due to the remote fires using the filled AOD along with surface PM2.5 measurements and other meteorological variables.

2 Data and Study Area

2.1 Study area

We estimated daily mean surface PM2.5 at 0.1-degree spatial resolution over Continental US (CONUS) from August 9th to 25th, 2018. The study area (inner domain) focuses on the US (25-50° N, 64-125° W), while the outer domain of the same WRF simulation extends to Canada (25-67° N, 70-140° W) to account for Canadian fire emissions and their contributions to US pollution from remote fire sources. Therefore, we chose August 2018 as our study period to analyze the impact of wildfires

on surface air pollution in the US based on the total fire radiative power calculation based on our previous work (Xue et al., 2021).

2.2 Ground-level PM2.5 observations

We obtained the daily surface PM2.5 concentration product that uses Federal Reference Methods and Federal Equivalent Methods (FRMs and FEMs, with code 88101) from US Environmental Protection Agency (EPA) for CONUS within the study period (https://www.epa.gov/outdoor-air-quality-data/). The measured frequency of each site is different (with a measurement interval of every 1, 3 or 6 days). A total of 950 EPA sites are available with approximately 71.1% sampling for daily data within the study period. Note that we discarded all PM2.5 values lower than the established detection limit of 2 $\mu g m^{-3}$ (EPA, 2018).

2.3 Satellite data

AOD values retrieved from satellite observations which is a columnar value of aerosol extinction, are correlated with surface pollution under certain conditions (Wang and Christopher, 2003; Hoff and Christopher, 2009). The relation between AOD and surface PM2.5 can be expressed as the following equation (Koelemeijer et al., 2006):

$$AOD = PM_{2.5} H f(RH) \frac{3 < Q_{ext,dry} >}{4 \rho r_{eff}} \tag{1}$$

From the above equation, several factors that bridge AOD and PM2.5, including: aerosol layer height H, particle effective radius r_{eff}, aerosol mass density ρ, extinction efficiency under dry conditions $Q_{ext,dry}$, and the ratio of ambient and dry extinction coefficients f(RF). Thus satellite AOD retrievals are often used as a vital indicator for estimating surface pollution (Hu et al., 2014; Xie et al., 2015).We use the 550nm AOD from the Multi-Angle Implementation of Atmospheric Correction (MAIAC MCD19A2 collection 6 product) with 1-km spatial resolution (https://lpdaac.usgs.gov/products/mcd19a2v006/). The product retrieves AOD from Terra and Aqua MODIS (Moderate Resolution Imaging Spectroradiometer), and we take the mean value of all available retrievals. Considering that thick smoke is likely misclassified as clouds, we accept all AOD with or without adjacent clouds (Xue et al., 2021; Goldberg et al., 2019). Through validation with AERONET AOD, the accuracy of the MAIAC AOD product is approximately 66% within the expected error (±0.05 ±0.1 AOD) (Lyapustin et al., 2018). The 1-km resolution AOD is gridded to 10 km by averaging all valid AOD values in 0.1-degree boxes. It is worth noting that MAIAC AOD is originally retrieved at 470nm and then computes the 550nm AOD using spectral properties (Lyapustin et al., 2018; Liu et al., 2019). It has also been reported that the uncertainties and biases increase with increasing AOD (Martins et al., 2017; Qin et al., 2021).

2.4 Meteorological data

The AOD-PM2.5 relationship depends on various factors, including meteorological parameters (Xue et al., 2021). Boundary layer height (BLH), 2-meter temperature (T2M), 10-meter wind speed (U10M), surface relative humidity (RH), and surface pressure (SP) were obtained from the European Centre of Medium-Range Weather Forecasts (ECMWF) Re-analysis (https:

To match the AOD data with an average value of two different times (10:30 am and 1:30 pm), we downloaded all meteorological variables at 12 pm local time. The spatial resolution of all meteorological data is 0.25 degrees, and we use the inverse distance method to interpolate all the variables to 0.1-degree spatial resolution.

3 WRF-Chem model and experimental design

The Weather Research and Forecasting model coupled with Chemistry (WRF-Chem V4.2.2) is applied in this study to examine the various processes that affect the transport of smoke aerosol and estimate the pollution change in the US due to Canadian fires. This section briefly describes the WRF-Chem model, the model configuration, and model physics and then introduces the design of the numerical experiments.

3.1 WRF-Chem model

WRF is a state-of-art mesoscale numerical weather prediction system that offers operational forecasting a flexible and computationally-efficient platform (Skamarock et al., 2019). WRF-Chem is an atmospheric chemistry model that fully integrated with the meteorological framework of WRF (Powers et al., 2017), enabling the simulation of various chemical and physical processes related to aerosol transport, including dispersion, aerosol-cloud interactions, and other key mechanisms (Powers et al., 2017).

3.2 Model configuration

There are several gas-phase chemistry and aerosol treatments available in WRF-Chem V4.2.2. In the current study, the Model of Ozone and Related chemical Tracers Version 4 (MOZART V4) gas-phase mechanism (Emmons et al., 2010; Knote et al., 2014) is used in combination with the MOdel for Simulating Aerosol Interactions and Chemistry (MOSAIC) 4-bin aerosol scheme (Zaveri et al., 2008). Four size bins (0.039-0.156, 0.156-0.625, 0.625-2.500, and 2.5-10.0 μm dry diameters) are used in the MOSAIC aerosol module for the representation of the aerosol size distribution. The PBL scheme used in our simulation is Mellor-Yamada-Janjic (MYJ) turbulent kinetic energy (TKE) scheme (Janjić, 1990, 1994) and the land-surface model scheme is the Noah Land Surface Model scheme (Chen and Dudhia, 2001). The cumulus scheme is the Grell 3D cumulus scheme (Grell and Dévényi, 2002), which performs better than other schemes (Hasan and Islam, 2018). The cloud micro-physics scheme is the Morrison 2-moment microphysics scheme (Morrison et al., 2005; Morrison and Pinto, 2005). Model radiation treatment utilizes the Rapid Radiative Transfer Model for General Circulation Models short-wave and long-wave radiation schemes (RRTMG,(Iacono et al., 2008)), including the aerosol radiation feedback.

Meteorological initial and lateral boundary conditions for WRF-Chem simulation are obtained from the National Centers for Environmental Prediction (NCEP) Global Data Assimilation System (GDAS) Final analysis (FNL) at 0.25-degree spatial resolution and 3-hour temporal resolution. The initial and lateral conditions of chemical species are obtained from the Whole Atmosphere Community Climate Model (WACCM) at 0.9*1.25-degree resolution with 88 levels. Key species associated with wildfires are included: Carbon monoxide (CO), carbon dioxide (CO2), black carbon (BC), nitrous oxide (N2O), nitrogen oxides (NOx) and so on (Mills et al., 2016). In addition, the Fire Inventory from NCAR version 2.4(FINNv2.4) is used as fire

emission input for the simulation. The model simulation was conducted over two nested domains: an outer domain covering the Canadian region (25-67° N, 70-140° W) and an inner domain focused on the CONUS region (25-50° N, 64-125° W). The simulation spanned August 9th-25th, 2018, with a spatial resolution of 10km for the inner domain and 71 vertical layers from surface to TOA (top of atmosphere). More details of the model configurations are shown in table 1.

Option type	Selected option
Horizontal grid resolution	10km (550*300)
Number of vertical layers	71 (39 layers below 2km)
Microphysics scheme	Morrison 2-moment scheme (Morrison et al., 2005; Morrison and Pinto, 2005)
Short and longwave radiation	RRTMG (Iacono et al., 2008)
Land surface	Noah-MP (Chen and Dudhia, 2001)
Boundary layer scheme	MYJ TKE scheme (Janjić, 1990, 1994)
Cumulus physics	Grell 3D (Grell and Dévényi, 2002)
Aerosol feedback	Yes
Chem-opt parameter	MOZART-MOSAIC (Emmons et al., 2010; Knote et al., 2014)
Meteorological data input	NCEP
Biogenic emissions	MEGAN
Anthropogenic emissions	EDGAR-2010

Table 1. Parameterizations used in WRF-Chem model simulations

4   Methods

This section mainly described the methods we used to estimate pollution changes in the Continental United States due to long-range transported smoke. We first described the method we used for filling the AOD gaps of the MAIAC satellite AOD product, then described two different methods for estimating surface PM2.5. Finally, we discuss how we assess the surface pollution change due to Canadian wildfires.

4.1   Filling the AOD gaps

To reiterate, one of the goals of the study is to estimate daily surface PM2.5 at 0.1-degree spatial resolution. AOD alone cannot provide necessary spatial coverage due to gaps in cloud cover. Therefore, we explored two commonly used methods for filling the AOD gaps. One commonly used method for daily AOD gap-filling problems is Kriging interpolation (Kianian et al., 2021; Singh et al., 2017). At the same time, the performance of Kriging interpolation degrades with increasing distances from the training points, which implies a limitation of the method in large areas of missing data (Kianian et al., 2021). Therefore, in the second method, we combine the Kriging method with outcomes from our CTM simulations to improve the AOD-gap interpolation.

4.1.1 Kriging interpolation

The ordinary Kriging (OK) method computes the estimation of an unsampled point based on the weighted average of surrounding pixels (Zandi et al., 2011). Several authors have fully described the theoretical basis of this method (Cressie, 1988; Emery, 2005), and has been proved to successfully fill in the AOD gaps for air pollution studies (Ma et al., 2014). The estimated AOD value at an unsampled location (x0) can be expressed as:

$$Z'(x_0) = \sum_{i=1}^{n} \lambda_i Z(x_i) \tag{2}$$

where i=1,2,3...n representing for the surrounding pixels, and λ_i is the kriging weight. A major factor that expresses the spatial dependence between neighboring points is the variogram (Arslan, 2012), which is defined as:

$$\gamma_h = \frac{1}{2n} \sum_{i=1}^{n} [Z(x_i) - Z(x_i + h)]^2 \tag{3}$$

where $Z(x_i)$ is the AOD value at point i and $Z(x_i + h)$ is the AOD value of other points that have a discrete distance h from point i. Previous studies have applied OK method with exponential variogram (or semi-variogram) on interpolating missing AOD values (Lv et al., 2016; Hu et al., 2019). Therefore, in this study, we use the OK method with exponential variogram to obtain a first-stage gap-filling daily AOD over our study area.

4.1.2 CTM interpolation

We applied the Kriging method for interpolation in areas with sufficient AOD information, while using CTM interpolation where valid AOD retrievals were unavailable, to minimize uncertainties associated with small-scale "missingness" of AOD. These uncertainties arise because CTM relies on fire inventories derived from satellite fire detection products, which may fail to capture small-scale fires due to the spatial resolution of satellite observations and fractional fire coverage within a pixel (Fu et al., 2020). Such undetected fire sources can lead to inaccuracies in CTM outputs. To better represent the AOD distribution in regions with small-scale "missingness," we prioritize the Kriging method over CTM interpolation. Therefore, our gap-filling method accepts kriging interpolation in regions with a small missing portion (<20%). At the same time, we feed the interpolation with CTM outputs for regions with a more significant missing portion. The details of the process are shown in figure 1.

To estimate the AOD value for a location without valid MAIAC AOD, we first select a 9×9-pixel box (spatial resolution of 0.1-degree) centered on the target pixel. Within this box, we identify pixels that satisfy two conditions: (a) having valid MAIAC AOD data, and (b) having a small AOD_{wrf} difference (0.1) compared to the target pixel. If fewer than 50 pixels meet these criteria, the box radius is expanded, and the filtering process is repeated. Once at least 50 pixels are identified, we calculate the ratio of valid MAIAC AOD pixels to the total number of pixels in the box, where total pixels refer to all pixels in the selected box, regardless of filtering. If the ratio exceeds 80%, the AOD for the target pixel is estimated using the ordinary kriging

200 (OK) method, based on the filtered pixels. However, if the ratio is 80% or lower, the AOD is calculated using a geographically weighted regression method that considers the neighboring ratio between MAIAC AOD and AOD_{wrf}:

$$AOD(x_0) = AOD_{wrf}(x_0) * R \tag{4}$$

where R is the weighted ratio which can be expressed as:

$$R = \sum_{i=1}^{n} (\alpha * w) \tag{5}$$

205 $$\alpha = \frac{AOD_{MAIAC}(x_i)}{AOD_{wrf}(x_i)} \tag{6}$$

$$w = \frac{1 - \frac{distance(x_i, x_0)}{bandwidth}}{\sum_{i=1}^{n}(1 - \frac{distance(x_i, x_0)}{bandwidth})} \tag{7}$$

Where $distance(x_i, x_0)$ means the distance between location x_i and x_0, and the bandwidth is selected based on the maximum distances between point x_i with valid MAIAC AOD and target pixel x_0 within the pre-selected box. According to above equations, we can obtain the AOD prediction for the unsampled location x_0.

210 ## 4.2 Estimating surface PM2.5 using the gap-filled AOD

Having the gap-filled AOD data, we can now estimate the surface PM2.5 with more extensive spatial coverage. In this study, we tested two methods (GWR and RF) for predicting surface PM2.5 using the gap-filled AOD with other meteorological variables. Due to characteristics of the regional wildfires, we chose both methods to consider spatial variations of pollution distribution. After comparing the fitting and validation results of the two methods, we apply the method with the better performance to

215 estimate daily surface PM2.5.

Before we perform the prediction, different data sets need to be resampled to the exact grid resolution. Grids with 0.cru1-degree spatial resolution are constructed over the study region. For AOD data with 1km resolution, we average all valid AOD values that fall into the same grid. Moreover, for other meteorological variables with a 0.25-degree resolution, we apply the inverse distance method to scale up all the variables into the predefined grids. PM2.5 measurements in the same grid are

220 averaged to one value to obtain a 0.1-degree resolution. In order to derive the relation between PM2.5 and AOD, we select data where AOD and surface PM2.5 are both available (AOD $>$ 0 AND PM2.5 $> 2.0 \mu gm^{-3}$) to train the models.

4.2.1 GWR method

To derive the surface PM2.5 using filled AOD with other meteorological variables, we used a GWR model that we fully describe in our prior work (Xue et al., 2021). The GWR model has advantages over other methods because it estimates spatially varying

relationships. The disadvantage of GWR model, on the other hand, is that the coefficients change daily according to different spatial characteristics of surface pollution, indicating increased computational expenses. To account for varying degrees of freedom centered on different locations, Adaptive bandwidth, selected by the Akaike's information criterion (AIC), is used for the GWR model. The model can be described as:

$$PM_{2.5,i,t} = \beta_{0,i,t} + \beta_{1,i,t}AOD_{i,t} + \beta_{2,i,t}BLH_{i,t} + \beta_{3,i,t}T2M_{i,t} + \beta_{4,i,t}U10M_{i,t} + \beta_{5,i,t}RH_{i,t} + \beta_{6,i,t}SP_{i,t} + \epsilon_i, t \qquad (8)$$

Where i represents different locations, t for different days, and β stands for the weight coefficients for different variables. The value of β depends on the geographical weighting of surrounding observations within the bandwidth. The weighting of each observation point decreases according to an exponential curve as the distances from the target point increase.

To test the GWR model, we must preserve only a small portion of the data, leaving most data to train the model since GWR requires an adequate number of samples, and the distribution of ground observations is uneven across the nation. Leave-one-out cross-validation (LOOCV) can be a relatively accurate way to test the model, but it requires much computational cost (Xue et al., 2021). Additionally, k-fold cross-validation with large fold numbers shows similar results (Xue et al., 2021). Therefore, we performed 100-fold cross-validation to evaluate the model performances. The entire inputs for the model are split into 100 subsets, and each time, we use one subset as testing samples while the other 99 subsets as fitting samples, after repeating this process 100 times until we test the whole data set. Finally, we evaluate the model performance by comparing the correlation coefficient (R), and root mean squared error (RMSE) of model fitting and cross-validation.

4.2.2 Random Forest method

Random forest is a non-parametric model that conducts estimations of prediction values by constructing a large number of decision trees. RF randomly divides nodes into sub-nodes for each tree, and the average estimation of different trees makes up the final results (Jiang et al., 2021a; Breiman, 1996). Of various machine learning methods, RF usually outperforms other machine learning methods due to its simplicity, diverse applications, tackling with complex cross-sensitivities among various features (Gupta et al., 2021; Jiang et al., 2021a; Zimmerman et al., 2018). The two vital parameters that affect the model performance is the tree number in the forest and feature numbers. We use 100 trees and six features in this study.

For our study period, a total of 11,942 samples are collected for training the model. The number of variables is the same as inputs for the GWR model in order to maintain consistency (AOD, BLH, T2M, U10M, RH, SP, latitude, longitude and day number). We also performed the same cross-validation as the GWR model to test the model performance so that the prediction accuracy can be compared between the two models. The model that performs better is selected to estimate the surface PM2.5 for locations where no PM2.5 observations are available based on: (a)the results of the cross-validation and (b)the differences of results (RMSE and correlation coefficients-R) between model fitting and validation. Note that a lower RMSE and higher R indicate high prediction accuracy, and a slight difference in model fitting and validation means the model is not over-fitting.

4.3 Assessing the pollution increase caused by Canadian fires

The model that performs better from the previous step is used for estimating the gaps in surface PM2.5. To further assess the surface pollution change due to long-range transported smoke from Canadian wildfires, we conduct a control run of WRF-Chem with all fire emissions within Canada turned off while emissions in the US are kept the same. The simulated surface PM2.5 of the control run (hereafter $PM_{2.5,control}$) and Canadian fire run (experiment run, $PM_{2.5,experiment}$) is then converted to surface PM2.5 based on the relation derived from previous steps:

$$PM_{2.5,control} = PM_{2.5} * \frac{PM_{2.5,WRF,control}}{PM_{2.5,WRF,experiment}} \tag{9}$$

where $PM_{2.5}$ is the estimated PM2.5 concentration using the better performed model (GWR or RF). The differences between $PM_{2.5,control}$ and $PM_{2.5}$ are then calculated to quantify the pollution change due to long-range transported smoke.

5 Results

5.1 Smoke plumes from Canadian wildfires transport to the US

Figure 2 shows the AOD change due to Canadian wildfires from August 17th to 20th, 2018. The changes in AOD distribution with and without Canadian fires vary according to wind directions and fire sources. The AOD change during the study period varies between 0 and 2.2 based on the two WRF-Chem simulations. The change is most prominent in North Dakota and Minnesota on August 17th, and the Canadian smoke continued to move southward to Iowa on August 18th. In the meantime, a large amount of Canadian smoke increased (high AOD increase) in Northwestern US (including Washington and Montana). On August 19th, Canadian smoke over the northwestern US was transported eastward, and more smoke was brought to the central US. On August 20th, Canadian smoke moved further to southern regions due to a storm system while the AOD values decreased, due to precipitation.

Canadian wildfire smoke has been consistently identified as a contributor to AOD increases across the US during wildfire seasons. For example, during a 2015 Canadian wildfire event, AOD increases exceeding 1 were observed along the eastern US coast (Yang et al., 2022). In a 2016 event, aerosol height data revealed that Canadian smoke contributed 40%–60% of the total column AOD in New York (Wu et al., 2018). Observed AOD increases for high-altitude aerosols from Canadian fires ranged from 0.18 to 0.45 at 532 nm in New York during this period. These findings align with the AOD increases simulated in our study and underscore the significant role of long-range transported Canadian smoke in contributing to regional pollution during wildfire episodes.

5.2 Associations of smoke transport with synoptic scale pressure patterns

Prior studies show that the transport of smoke aerosols is usually affected by synoptic pressure patterns. High surface pressure often indicates the accumulation of surface pollution, while successive low pressure can also increase surface pollution (Chen

et al., 2008). In order to investigate the relationship between synoptic pressure patterns and the smoke transport process, we compared the horizontal and vertical distribution of Canadian smoke in the US.

According to the surface pressure map on August 17, 2018 (as shown in Figure 3a), there was a high-pressure system located in Ontario, and its influence extended into parts of North Dakota. This high-pressure system was moving eastward, and as it moved east, the descending air associated with the high-pressure system inhibited vertical convection, leading to the entrapment of smoke in the lower atmosphere. Consequently, the smoke experienced dry deposition at lower altitudes, which explains the low AOD concentration over northeastern Minnesota in figure 2a. Smoke at higher altitudes tended to be redirected around the high-pressure system. Simultaneously, there was a low-pressure system situated in the North Wisconsin region, causing the smoke to move in a northeasterly direction towards this low-pressure area. On August 18th, as shown in Figure 3b, the high-pressure system shifted to Quebec, and its peripheral influence extended to the Madison region. This presence of the high-pressure system resulted in the formation of a narrow corridor of low AOD distribution within the path of smoke transport, as illustrated in Figure 2b. On the same day, a low-pressure system was forming over South Dakota and Nebraska. The ascending air and the robust winds along the trough axis established more conducive circumstances for the transportation of Canadian smoke. This phenomenon is clearly illustrated in figure 2c, where the smoke expanded further to the south, strongly influenced by the presence of the evolving low-pressure system. By August 20th, this system had transitioned eastward, enveloping the states of Iowa and Missouri, as in figure 3d. Intense rainfall and thunderstorms materialized as the low-pressure system rotated over the area. This precipitation served as a scavenging mechanism, effectively eliminating the smoke through a wet deposition process. Some portions of the smoke, however, carried by the powerful winds, could potentially impact air quality in the southern regions.

Figure 4 shows the surface PM2.5 distribution from EPA stations during the four days, while figure 5 presents the surface PM2.5 dry mass contributed solely by Canadian wildfires, as derived from the difference between the Canadian fire case and the control case in WRF-Chem simulations. Comparing these figures helps distinguish the contributions of local sources and long-range transported Canadian wildfire smoke to surface pollution in the United States. If regions of high PM2.5 in Figure 4 correspond to low values in Figure 5, it suggests that pollution in those areas is predominantly caused by local sources. Conversely, if high values in Figure 4 align with elevated values in Figure 5, it indicates that Canadian wildfire smoke is a significant contributor. On August 17th, elevated surface PM2.5 levels (>10 $\mu g m^{-3}$) were observed in northern US states. However, in the difference map, areas such as Montana, North Dakota, and South Dakota exhibit low values close to zero, indicating that surface pollution in the northwestern US primarily originated from local fires. On August 18th, a high-pressure system positioned over Minnesota resulted in higher surface PM2.5 concentrations in that region. However, the difference map shows low values over the same area, indicating that the elevated pollution levels were primarily due to local sources. High-pressure systems typically feature calm winds and stable atmospheric conditions, which trap pollutants near the surface and hinder the transport of Canadian wildfire smoke into the region. By August 19th (Figure 4c), surface PM2.5 levels increased across central US states, with high AOD concentrations noted over Utah and Illinois, likely influenced by high-pressure systems. In contrast, elevated PM2.5 levels in Iowa and Missouri appear to align with the transport of Canadian wildfire smoke. A low-pressure system extending southward facilitated the movement of smoke, reaching as far south as

11

Missouri, thereby expanding the range of smoke transport compared to the preceding days. The impact of the low-pressure
320 system became more pronounced on August 20th (Figure 4d). In the center of the cyclone, particularly in Iowa and Missouri,
wet deposition processes dominated. The robust winds associated with the low-pressure system carried Canadian smoke, which
was subsequently removed by precipitation, leading to no significant increase in surface pollution in these areas. However,
along the outer boundaries of the cyclone, from Colorado through Kansas and Oklahoma to northern Texas, surface pollution
levels noticeably increased. This increase can be attributed to Canadian smoke transported by the strong winds of the low-
325 pressure system, resulting in heightened PM2.5 concentrations in these regions.

With low-pressure systems in the central US, both model outputs and surface observations show longer southward transport
paths of Canadian smoke in the US. Take August 20th as an example; air flows of the extratropical cyclone in Iowa state sub-
stantially determine the transport direction of the Canadian smoke. To investigate smoke's horizontal and vertical transport, we
take the pollution distribution map of three atmospheric layers (773hPa, 850hPa, and 900hPa) to compare the moving direc-
330 tions of smoke (figure 6). In upper layers (773hPa), Canadian smoke intrudes into the US from two directions: northwestern US
and northeastern US. These two smoke plumes meet in the central US at higher level and then split into two directions while
transporting downward (as shown in the black circles at 900hPa map). The downward transport directions can be explained
using a conceptual model of the extratropical cyclone (figure 6(d)). Canadian smoke follows the downward airflow: part of the
smoke moves southwesterly away from the cyclone while the rest of the pollution moves toward the cyclone and goes through
335 wet deposition processes.

Overall, the horizontal distribution and transport of Canadian smoke are closely related to pressure systems. Surface high
pressure usually facilitates the subsidence of elevated Canadian smoke pollution (with surface PM2.5 increase). In contrast, a
low-pressure system tends to have the opposite effect (lifting), corresponding to longer transport distances.

5.3 Daily coverage of satellite AOD and simulated AOD from WRF-Chem

340 During the wildfire period selected in this study (17 days), we calculate the daily MAIAC AOD coverage using the number
of pixels with valid AOD values divided by the total number of pixels. The AOD coverage after combining Aqua and Terra
data ranges from 46% to 68% (shown in figure 7). Analyzing daily AOD coverage is essential, as satellite-derived AOD
serves as a columnar indicator of pollution with extensive spatial coverage and high-resolution data, making it a valuable
predictor for estimating surface PM2.5 concentrations alongside other variables. However, it often has missing values over
345 fire-intense regions, which can significantly impact the accuracy of predicted surface PM values. Using Model-simulated AOD
in conjunction with satellite AOD can help mitigate this issue and improve predictions.

In order to show the spatial distribution of AOD coverage, we also calculate the coverage ratio of AOD of each pixel in the
17 days (shown in figure 8). The average AOD coverage for the whole study area is around 60%. For the northeastern US,
40%-70% of the days are covered by clouds, while more than 80% of the days have valid AOD values in the western US.
350 The model simulated 550nm AOD has a very similar distribution as the satellite AOD. Comparing MAIAC AOD with
corresponding simulated AOD pixels, the correlation coefficients range from 0.3 to 0.63, and the RMSE is within the range
of 0.2-0.4 (shown in table S2). Time series of the coverage and statistics are shown in figure 7. There are no clear correlation

between MAIAC AOD coverage and the correlation of two AOD products, as the missing AOD areas for each day are randomly distributed affected by satellite swath coverage and cloud contaminations. Overall, simulated AOD is lower than satellite AOD

355 potentially due to underestimation of fire emissions, especially for small-scale fires (Wiedinmyer et al., 2011). FINNv2.4 identified fire sources based on the combinations of thermal anomalies product of MODIS and VIIRS (Visible Infrared Imaging Radiometer Suite) (Wiedinmyer et al., 2011; Li et al., 2021). Adding high spatial resolution fire detection information from VIIRS increases the total burned area by 280% compared to the previous FINN version that used MODIS detection only (Li et al., 2021). However, thick smoke and cloud cover primarily affect the detection of fires (Fu et al., 2020; Schroeder et al.,

360 2014), causing AOD underestimation in regions with missing fire detection.

The comparison between WRF simulated AOD and satellite retrieved AOD shows high spatial correlation, indicating similar smoke pathway between the model and satellite observations. We also compare the ground AERONET AOD with the model simulated values. The correlation coefficient during the 17 days between two AOD product is 0.54, and the RMSE is around 0.06. Similar to the comparison with satellite AOD, model simulated AOD values show underestamations compared to

365 AERONET AOD.

5.4 AOD gap filling

Our gap-filled AOD increased the mean coverage from 60% to 92%, and missing values of the gap-filled AOD were mainly distributed at the edges of our study area due to limited satellite retrieval to derive accurate $AOD_{filled} - AOD_{MAIAC}$ relationships.

370 To illustrate the importance and differences of feeding the interpolation with CTM outputs, we choose August 13th to display the differences when fires are detected near cloud edges. Figure 9 shows the AOD distribution of the CTM-filled AOD, kriging-filled AOD, and MAIAC AOD. The south-central US region (including Texas, Oklahoma, and Nebraska) has large missing AOD areas due to clouds. The kriging-filled AOD for this region is evenly distributed with values around 0.3. However, the CTM-filled AOD shows more variations and a clear smoke transport path along the wind direction. The primary

375 reason for this difference is some small-scale fires detected near the cloud edges in Oklahoma. According to the fire emission document (https://www.acom.ucar.edu/Data/fire/data/finn2/README_FINNv2.5_Feb2022.pdf), both 375m resolution VIIRS fire detection and 1km resolution MODIS thermal anomalies are used for estimating fire emissions. This enhancement in fire detection provides a more accurate estimation of surface pollution in the presence of clouds. Compared with the surface PM2.5 distribution of this same day, we find the same distribution pattern as our CTM-filled AOD: high PM2.5 ($> 20 \mu g m^{-3}$)

380 distributed in central Texas all the way to Eastern Oklahoma. Therefore, CTM-filled AOD provides closer patterns as observed surface pollution distribution at regions with large cloud covers. Our results indicate the inadequacy of kriging methods in such cases.

5.5 Daily PM2.5 estimation

Figure 10 shows the GWR model fitting and cross-validation results. The colors represent the probability function that deter-

385 mines the possibility that the ground-level measurements and the estimations from the GWR model are equal to each other.

13

Lighter color means a higher concentration of samples. The R and RMSE of the GWR fitting model are 0.85 and 6.2 μgm^{-3}, respectively, and the R and RMSE of the 100-fold cross-validation are 0.8 and 7.2 μgm^{-3}. The difference between model fitting and cross-validation is relatively small, which means that the model is not overfitting and the prediction accuracy is stable. The slope of the cross-validation best-fit line (solid black line) is 0.72, indicating that the model slightly underestimates the surface PM2.5, and the biases increase with increasing AOD. The reason for this underestimation is sample biases: 1) a limited number of stations in the Western US; 2) EPA station distribution in the Western US mainly concentrates in the two populated regions, showing extremely uneven distribution. Only 3% surface PM2.5 observations exceed the unhealthy limit (PM2.5 $35.5\mu gm^{-3}$) during the 17 days, and among these stations, 62% of the observations came from stations located in Washington and California.

Figure 11 shows the results for RF fitting and cross-validation. RF model fits well with the training samples with R of 0.84 and RMSE of 6.56 μgm^{-3}, while the cross-validation results degrade significantly (R=0.76, RMSE=7.69 μgm^{-3}). The slope of the validation best-fit line is 0.523, which is of lower than the GWR method. The difference between model fitting and cross-validation indicates that the model is slightly over-fitting and has limited prediction accuracy for this case. One possible reason for this could be the limited number of training samples with average daily available measurements of around 700 during the study period (Jiao et al., 2021). A space-time RF model can be utilized to enhance RF model performance (Wei et al., 2019). Compared with RF, the GWR model showed slightly higher prediction accuracy and more stability.

Though the difference in cross-validation results for RF and GWR is slight, the daily pollution variation estimated from the two methods shows completely different trends. Figure 12 shows the mean PM2.5 variation over the three highly polluted areas (EPA Region 8,9,10) during the 17-day period calculated from GWR, RF, and EPA ground stations. For region 8, EPA stations measured two pollution peaks during the study period: one peak on August 19th and another smaller peak on August 24th. Mean PM2.5 from the RF method also captured the two peaks on the same day, while the regional mean values were slightly lower than the measurements. However, GWR has a different peak on August 11th but no noticeable increase for the remaining days. For EPA Region 9, both RF and EPA stations show a decreasing trend for the first few days and then slowly increase with time, while GWR has two clear peaks, which are not shown for the other two methods. For the most polluted region 10, the highest peaks from August 19th to 22nd are shown in EPA and RF method, but GWR shows low values for the same period. The differences between GWR and RF methods come from the distribution of sample points. In Region 10, most EPA stations are located in Washington state, meaning pollution increases there strongly influence the regional mean PM2.5 when using RF. Conversely, GWR sometimes captures variations in other areas, even when station coverage is sparse. RF is more sensitive to the spatial distribution of ground stations, with its regional mean values closely aligning with EPA station trends. In contrast, GWR is more effective at detecting PM2.5 variations in areas with limited station coverage. An even distribution of samples could significantly improve estimation accuracy for both methods. Given the observed pollution trends across these highly affected regions, GWR was selected to estimate surface PM2.5 in this study.

Our GWR daily mean estimation of surface PM2.5 during the 17-day wildfire event for each EPA region ranges from 3.1 to 60.2 μgm^{-3} (shown in table 2). The mean surface pollution is highest at region 10 while lowest at region 1, which is comparable with previous study (Xue et al., 2021).

Date	Region1	Region2	Region3	Region4	Region5	Region6	Region7	Region8	Region9	Region10
Aug-10	6.9	7.5	7.4	7.5	9.1	10.6	8.5	15.4	27.0	28.4
Aug-11	10.5	11.7	13.3	9.7	10.3	9.1	9.8	15.9	12.4	22.1
Aug-12	5.1	5.8	6.9	6.8	12.8	8.9	11.0	15.0	13.0	26.9
Aug-13	6.2	5.9	5.8	7.1	12.7	10.6	15.3	32.4	14.7	46.4
Aug-14	6.3	5.9	6.5	6.6	12.8	10.7	14.8	16.6	13.3	60.2
Aug-15	5.9	5.7	5.9	7.0	11.4	11.1	16.6	14.0	20.0	44.3
Aug-16	3.1	6.4	8.8	10.1	11.2	11.3	16.1	14.3	15.0	40.6
Aug-17	5.5	6.9	8.9	12.8	12.7	10.2	15.3	19.4	13.4	34.9
Aug-18	11.3	11.6	9.6	13.2	9.1	11.5	16.6	22.5	15.5	29.9
Aug-19	14.5	12.2	10.9	13.2	13.4	11.3	15.4	19.0	15.4	20.5
Aug-20	7.1	8.3	8.3	7.5	11.9	10.2	9.4	20.6	26.4	30.9
Aug-21	6.9	8.7	9.8	9.3	14.1	12.2	13.0	17.2	19.6	24.9
Aug-22	5.1	6.4	8.3	9.0	16.2	12.4	15.1	16.1	16.9	18.0
Aug-23	5.3	5.5	8.2	10.3	15.9	13.9	14.9	16.5	13.5	14.6
Aug-24	6.0	6.0	7.0	10.9	15.5	14.8	13.5	18.5	14.1	25.8
Aug-25	5.3	6.6	8.1	12.1	15.1	13.5	13.9	17.5	13.9	32.9
Aug-26	7.8	13.0	13.4	14.5	13.9	13.5	12.4	15.6	12.6	35.4

Table 2. Mean PM2.5 concentrations ($\mu g m^{-3}$) over different EPA regions (1-10) estimated using GWR method

5.6 Pollution change due to long-range transported smoke from Canada

Using coefficients derived from simulated PM2.5 in control and experiment scenarios, we estimated the PM2.5 increase attributed to Canadian wildfires. Table 3 presents the daily mean PM2.5 increase across different EPA regions. The regional mean PM2.5 increase reached up to 28 μg/m^3, with Canadian wildfire smoke contributing as much as 87.8% of total PM2.5.
Region 10 experienced the highest impact, while Region 1 was the least affected. Notably, on some days, the contribution of Canadian wildfire smoke to total PM2.5 in the Northeastern U.S. (Regions 1, 2, and 3) exceeded that in the Northwestern U.S. (Regions 8 and 10). The contribution of wildfire smoke to total PM2.5 closely followed wildfire activity patterns; however, due to transport distances, it often took time for smoke to travel from Region 10 to Region 1. As a result, during some wildfire episodes, PM2.5 changes in the Eastern CONUS lagged behind those in the Western CONUS by a day.

Due to the CAA, the overall trend of surface PM2.5 in the recent years is gradually decreasing (figure S1). The decreasing trend is evident in August mean PM2.5 calculated from EPA surface observations from EPA region 1 to region 7, but variations of PM2.5 in region 8 to 10 is more affected by the occurrence of wildfires. For years with low wildfire occurrences (FRP < 10000 MJ), August surface PM2.5 show a steady pattern in region 8 and region 10 without any apparent rising or dropping.

PM2.5 in region 9 shows descending pattern in August in years without large fires, while it can reach up to three times more
435 of the baseline in wildfire years. For regions 1 to 7, August mean PM2.5 concentrations decrease about 5% -10% each year in
different regions. Compared with table S1, the 17-day investigation highlights how long-range transported smoke from Canada
temporarily offsets the descending trend in surface PM2.5 during the study period. For regions 8 to 10, wildfires (including
contributions from both local and remote fires) increase the August mean surface PM2.5 by 0-98%. While this study focuses
on a short-term event, it demonstrates the significant seasonal impact of Canadian smoke on air quality, emphasizing the need
440 for multi-year investigations to assess long-term trends in Canadian smoke contributions.

In conclusion, due to the concurrent local and remote wildfires, the long-range transport smoke contributed to about half of
the surface pollution increase in EPA regions 8, 9, and 10. For other EPA regions, Canadian smoke compensated the CAA,
causing surface pollution to rise.

Date	Region1	Region2	Region3	Region4	Region5	Region6	Region7	Region8	Region9	Region10
Aug-10	34.3	39.1	39.1	43.9	59.9	64.3	63.7	48.6	26.2	18.1
Aug-11	8.5	15.8	16.7	19.4	0	26.1	17.1	32.2	33.5	36.8
Aug-12	0	0.1	0.5	6.7	21.0	28.8	26.1	8.6	13.6	4.2
Aug-13	1.7	6.0	8.5	7.7	17.6	4.1	0	0	0	8.9
Aug-14	1.0	0.7	0	0	5.0	1.7	3.0	3.5	1.7	1.2
Aug-15	4.9	-0.6	-6.9	-2.5	-2.1	0.1	1.4	12.4	16.1	24.3
Aug-16	48.8	40.6	41.9	51.6	67.2	62.9	67.2	74.1	67.0	69.0
Aug-17	65.0	68.4	74.3	77.7	81.5	71.6	77.6	64.3	53.9	54.8
Aug-18	62.8	60.9	61.0	66.6	69.7	67.3	68.7	51.9	50.3	54.3
Aug-19	57.1	59.6	62.9	64.0	66.7	66.3	66.9	63.9	58.9	67.5
Aug-20	13.0	23.0	24.1	24.1	18.9	33.3	17.2	18.1	35.0	23.5
Aug-21	23.6	19.9	26.3	26.7	26.3	14.8	25.5	22.1	11.2	16.9
Aug-22	52.6	60.2	64.3	69.1	59.1	73.5	69.2	46.0	63.9	22.3
Aug-23	62.0	63.6	75.6	80.1	87.4	85.6	86.6	87.8	85.2	86.3
Aug-24	66.4	69.5	71.9	79.1	69.6	76.1	67.8	75.1	73.7	85.0
Aug-25	55.4	56.2	54.6	53.9	56.4	62.5	53.3	62.3	68.5	65.5
Aug-26	52.3	51.6	59.5	67.3	49.2	67.6	59.6	51.5	66.1	52.3

Table 3. Percentage increase of PM2.5 concentrations (%) due to Canadian wildfires over different EPA regions (1-10) estimated using GWR
method

5.7 Uncertainties and limitations

The main uncertainties and limitations of this study come from the CTM model and various inputs of the model, and the surface pollution estimation model also leads to some uncertainties:

1) Since satellite fire detection is affected by various factors, including cloud cover, fire sizes and the background environment, emission inputs for the WRF-Chem simulations derived from the fire detection products introduces uncertainties into our simulations and create regional biases in the simulated AOD values.

2) In addition to the fire detection biases, assumption made in computing fire emissions also cause the following uncertainties that affect the simulations: a)fire sizes and duration; b)amount and distribution of biomass fuels; c)fraction of different emissions from the biomass fuel Soares et al. (2015). These factors may influence the mass concentration and distribution of smoke aerosols.

3)Uncertainties in the injection height of smoke plumes in WRF-Chem can impact simulation accuracy. Biases in injection height influence horizontal transport speed, direction, and pollution residence time, potentially introducing errors in the AOD gap-filling process. Moreover, uncertainties in the vertical distribution of aerosols can affect the AOD-PM2.5 relationship, with variations in plume height between monitors leading to inaccuracies in estimated surface PM2.5 concentrations.

4) The unevenly distributed EPA stations primarily affect the performance of the two pm2.5 estimation models, causing completely different daily variation trends of regional mean PM2.5. Therefore, the model performance may be improved if we use more EPA stations (We use FRM monitors only in this study).

5) Since we need the relationships between satellite AOD and CTM AOD to calculate the filled AOD values, the filling values cannot be derived if the area of missing satellite AOD is larger than the radius thresholds we set for deriving the relationships. For days with large areas of missing satellite AOD at the boundary region of our study region, we sometimes have missing AOD values at the boundary. This can be improved by increasing the radius thresholds or the study region to leave space for the boundaries.

6 Conclusion

This study first analyzed the influence of different physical processes on the transport of long-range transported smoke aerosols by comparing two WRF-Chem simulations with and without Canadian wildfires. Then we utilized the simulated AOD from CTM and Kriging interpolation with a geographically weighted method to fill in the daily AOD retrieval gaps caused by cloud covers. Then we estimated the surface PM2.5 concentration using GWR and RF methods and tested the two predictions using cross-validation and trend analysis to choose a better-performing method. Finally, by turning off the Canadian wildfire emissions in the CTM simulations, we calculated the surface PM2.5 concentrations from the CTM AOD outputs using the coefficients derived from previous estimations. The differences in PM2.5 of the two estimations indicated the change brought by long-range transported smoke from Canadian wildfires. The main findings of our study are:

1) Synoptic scale pressure systems are the dominant drivers of horizontal pollution transport pathways. In the meantime, the pressure systems can also affect the vertical distribution by ascending or descending smoke. Under most circumstances, the

subsidence flow of high-pressure systems facilitates the drifting process of elevated smoke layers and thus increases surface pollution. In contrast, the cyclonic storm system leads to a longer transport path (further south of CONUS in this study) and directs the elevated smoke to the ground in different directions. Therefore, the co-occurrence of low-pressure systems and smoke aerosols corresponds to larger pollution areas.

Certain weather patterns can facilitate the dispersion of smoke, hence, during severe wildfire events, it becomes crucial to closely monitor the meteorological conditions and alert the public about the potential risks of deteriorating air quality, even if the fires are hundreds of miles away. Furthermore, when conducting prescribed fire burning, it is essential to take into account the possibility of smoke being transported to densely populated areas. In other words, proper consideration of the weather conditions and potential wind patterns is crucial to minimizing the impact on nearby populations.

2) Daily AOD coverages combining Aqua and Terra MODIS range from 46% to 68% during our study period, and our filled AOD values using CTM AOD outputs are able to fill in the missing gaps.

3) Daily PM2.5 estimations using the filled AOD product with other meteorological data using the GWR method (R=0.8) perform better than the RF model (R=0.76), and the RF model captures the daily variations of different EPA regions calculated from EPA stations.

4) Regional mean increase of surface PM2.5 concentrations that came from Canadian wildfire smoke ranges up to 28 μgm^{-3} (a 69% increase), and EPA Region 10 is most affected by Canadian fires while region 6 is the least. The PM2.5 change pattern in Eastern CONUS often lags the Western CONUS by a day.

Our study found that presence of synoptic scale pressure systems leads to a higher proportion of CONUS region being affected by long-range transported smoke from Canada. Typical airflow patterns that are associated with extratropical cyclones are particularly effective at transporting elevated layers of smoke to the surface and fanning the associated particulate pollution over large areas. Such transport pathways associated with extratropical cyclones need to be considered when forecasting for the effects of smoke pollution from Canadian wildfires on vulnerable populations in the CONUS region. Our study highlights the significant contribution of wildfires to particulate pollution during the study period, aligning with prior research that suggests wildfires are becoming an increasingly important source of particulate pollution as industrial pollution declines due to stringent regulations (Xue et al., 2021). However, further multi-year investigations are needed to robustly confirm this trend on a broader temporal scale.

References

Aguilera, R., Corringham, T., Gershunov, A., and Benmarhnia, T.: Wildfire smoke impacts respiratory health more than fine particles from other sources: Observational evidence from Southern California, Nature communications, 12, 1–8, 2021.

Ahern, A., Robinson, E., Tkacik, D., Saleh, R., Hatch, L., Barsanti, K., Stockwell, C., Yokelson, R., Presto, A., Robinson, A., et al.: Production of secondary organic aerosol during aging of biomass burning smoke from fresh fuels and its relationship to VOC precursors, Journal of Geophysical Research: Atmospheres, 124, 3583–3606, 2019.

Akagi, S. K., Craven, J., Taylor, J., McMeeking, G., Yokelson, R., Burling, I., Urbanski, S., Wold, C., Seinfeld, J., Coe, H., et al.: Evolution of trace gases and particles emitted by a chaparral fire in California, Atmospheric Chemistry and Physics, 12, 1397–1421, 2012.

Aloyan, A., Arutyunyan, V., Lushnikov, A., and Zagaynov, V.: Transport of coagulating aerosol in the atmosphere, Journal of aerosol science, 28, 67–85, 1997.

Arslan, H.: Spatial and temporal mapping of groundwater salinity using ordinary kriging and indicator kriging: The case of Bafra Plain, Turkey, Agricultural water management, 113, 57–63, 2012.

Bai, Y., Wu, L., Qin, K., Zhang, Y., Shen, Y., and Zhou, Y.: A geographically and temporally weighted regression model for ground-level PM2. 5 estimation from satellite-derived 500 m resolution AOD, Remote Sensing, 8, 262, 2016.

Beaver, S., Palazoglu, A., Singh, A., Soong, S.-T., and Tanrikulu, S.: Identification of weather patterns impacting 24-h average fine particulate matter pollution, Atmospheric Environment, 44, 1761–1771, 2010.

Bowe, B., Xie, Y., Yan, Y., and Al-Aly, Z.: Burden of cause-specific mortality associated with PM2. 5 air pollution in the United States, JAMA network open, 2, e1915 834–e1915 834, 2019.

Breiman, L.: Bagging predictors, Machine learning, 24, 123–140, 1996.

Bu, X., Xie, Z., Liu, J., Wei, L., Wang, X., Chen, M., and Ren, H.: Global PM2. 5-attributable health burden from 1990 to 2017: Estimates from the Global Burden of disease study 2017, Environmental Research, 197, 111 123, 2021.

Carrico, C. M., Kreidenweis, S. M., Malm, W. C., Day, D. E., Lee, T., Carrillo, J., McMeeking, G. R., and Collett Jr, J. L.: Hygroscopic growth behavior of a carbon-dominated aerosol in Yosemite National Park, Atmospheric Environment, 39, 1393–1404, 2005.

Chen, F. and Dudhia, J.: Coupling an advanced land surface–hydrology model with the Penn State–NCAR MM5 modeling system. Part I: Model implementation and sensitivity, Monthly weather review, 129, 569–585, 2001.

Chen, J. and Hoek, G.: Long-term exposure to PM and all-cause and cause-specific mortality: a systematic review and meta-analysis, Environment international, 143, 105 974, 2020.

Chen, Z., Cheng, S., Li, J., Guo, X., Wang, W., and Chen, D.: Relationship between atmospheric pollution processes and synoptic pressure patterns in northern China, Atmospheric Environment, 42, 6078–6087, 2008.

Colarco, P., Schoeberl, M., Doddridge, B., Marufu, L., Torres, O., and Welton, E.: Transport of smoke from Canadian forest fires to the surface near Washington, DC: Injection height, entrainment, and optical properties, Journal of Geophysical Research: Atmospheres, 109, 2004.

Cotton, W. R., Bryan, G., and van den Heever, S. C.: The mesoscale structure of extratropical cyclones and middle and high clouds, in: International Geophysics, vol. 99, pp. 527–672, Elsevier, 2011.

Cressie, N.: Spatial prediction and ordinary kriging, Mathematical geology, 20, 405–421, 1988.

Damoah, R., Spichtinger, N., Servranckx, R., Fromm, M., Eloranta, E., Razenkov, I., James, P., Shulski, M., Forster, C., and Stohl, A.: A case study of pyro-convection using transport model and remote sensing data, Atmospheric Chemistry and Physics, 6, 173–185, 2006.

540 Emery, X.: Simple and ordinary multigaussian kriging for estimating recoverable reserves, Mathematical Geology, 37, 295–319, 2005.

Emmons, L. K., Walters, S., Hess, P. G., Lamarque, J.-F., Pfister, G. G., Fillmore, D., Granier, C., Guenther, A., Kinnison, D., Laepple, T., et al.: Description and evaluation of the Model for Ozone and Related chemical Tracers, version 4 (MOZART-4), Geoscientific Model Development, 3, 43–67, 2010.

EPA: Code of Federal Regulations Title 40: Protection of Environment, https://www.govinfo.gov/app/collection/cfr/2018/, 2018.

545 Fu, Y., Li, R., Wang, X., Bergeron, Y., Valeria, O., Chavardès, R. D., Wang, Y., and Hu, J.: Fire detection and fire radiative power in forests and low-biomass lands in Northeast Asia: MODIS versus VIIRS Fire Products, Remote Sensing, 12, 2870, 2020.

Geng, G., Zhang, Q., Martin, R. V., van Donkelaar, A., Huo, H., Che, H., Lin, J., and He, K.: Estimating long-term PM2. 5 concentrations in China using satellite-based aerosol optical depth and a chemical transport model, Remote sensing of Environment, 166, 262–270, 2015.

Goldberg, D. L., Gupta, P., Wang, K., Jena, C., Zhang, Y., Lu, Z., and Streets, D. G.: Using gap-filled MAIAC AOD and WRF-Chem to
550 estimate daily PM2. 5 concentrations at 1 km resolution in the Eastern United States, Atmospheric Environment, 199, 443–452, 2019.

Gomez, S. L., Carrico, C., Allen, C., Lam, J., Dabli, S., Sullivan, A., Aiken, A. C., Rahn, T., Romonosky, D., Chylek, P., et al.: Southwestern US biomass burning smoke hygroscopicity: The role of plant phenology, chemical composition, and combustion properties, Journal of Geophysical Research: Atmospheres, 123, 5416–5432, 2018.

Grell, G. A. and Dévényi, D.: A generalized approach to parameterizing convection combining ensemble and data assimilation techniques,
555 Geophysical Research Letters, 29, 38–1, 2002.

Gupta, P. and Christopher, S. A.: Particulate matter air quality assessment using integrated surface, satellite, and meteorological products: 2. A neural network approach, Journal of Geophysical Research: Atmospheres, 114, 2009a.

Gupta, P. and Christopher, S. A.: Particulate matter air quality assessment using integrated surface, satellite, and meteorological products: Multiple regression approach, Journal of Geophysical Research: Atmospheres, 114, 2009b.

560 Gupta, P., Zhan, S., Mishra, V., Aekakkararungroj, A., Markert, A., Paibong, S., Chishtie, F., et al.: Machine Learning Algorithm for Estimating Surface PM2. 5 in Thailand, Aerosol and Air Quality Research, 21, 210 105, 2021.

Hasan, M. A. and Islam, A.: Evaluation of microphysics and cumulus schemes of WRF for forecasting of heavy monsoon rainfall over the southeastern hilly region of Bangladesh, Pure and Applied Geophysics, 175, 4537–4566, 2018.

Hoff, R. M. and Christopher, S. A.: Remote sensing of particulate pollution from space: have we reached the promised land?, Journal of the
565 Air & Waste Management Association, 59, 645–675, 2009.

Hu, H., Hu, Z., Zhong, K., Xu, J., Zhang, F., Zhao, Y., and Wu, P.: Satellite-based high-resolution mapping of ground-level PM2. 5 concentrations over East China using a spatiotemporal regression kriging model, Science of the Total Environment, 672, 479–490, 2019.

Hu, X., Waller, L. A., Lyapustin, A., Wang, Y., Al-Hamdan, M. Z., Crosson, W. L., Estes Jr, M. G., Estes, S. M., Quattrochi, D. A., Puttaswamy, S. J., et al.: Estimating ground-level PM2. 5 concentrations in the Southeastern United States using MAIAC AOD retrievals and
570 a two-stage model, Remote sensing of environment, 140, 220–232, 2014.

Hu, X., Belle, J. H., Meng, X., Wildani, A., Waller, L. A., Strickland, M. J., and Liu, Y.: Estimating PM2. 5 concentrations in the conterminous United States using the random forest approach, Environmental science & technology, 51, 6936–6944, 2017.

Iacono, M. J., Delamere, J. S., Mlawer, E. J., Shephard, M. W., Clough, S. A., and Collins, W. D.: Radiative forcing by long-lived greenhouse gases: Calculations with the AER radiative transfer models, Journal of Geophysical Research: Atmospheres, 113, 2008.

575 Janjić, Z. I.: The step-mountain coordinate: Physical package, Monthly weather review, 118, 1429–1443, 1990.

Janjić, Z. I.: The step-mountain eta coordinate model: Further developments of the convection, viscous sublayer, and turbulence closure schemes, Monthly weather review, 122, 927–945, 1994.

Jiang, T., Chen, B., Nie, Z., Ren, Z., Xu, B., and Tang, S.: Estimation of hourly full-coverage PM2. 5 concentrations at 1-km resolution in China using a two-stage random forest model, Atmospheric Research, 248, 105 146, 2021a.

580 Jiang, Y., Xin, J., Wang, Y., Tang, G., Zhao, Y., Jia, D., Zhao, D., Wang, M., Dai, L., Wang, L., et al.: The thermodynamic structures of the planetary boundary layer dominated by synoptic circulations and the regular effect on air pollution in Beijing, Atmospheric Chemistry and Physics, 21, 6111–6128, 2021b.

Jiao, J., Chen, Y., and Azimian, A.: Exploring temporal varying demographic and economic disparities in COVID-19 infections in four US areas: based on OLS, GWR, and random forest models, Computational urban science, 1, 1–16, 2021.

585 Kianian, B., Liu, Y., and Chang, H. H.: Imputing satellite-derived aerosol optical depth using a multi-resolution spatial model and random forest for PM2. 5 prediction, Remote Sensing, 13, 126, 2021.

Kim, Y. H., Warren, S. H., Krantz, Q. T., King, C., Jaskot, R., Preston, W. T., George, B. J., Hays, M. D., Landis, M. S., Higuchi, M., et al.: Mutagenicity and lung toxicity of smoldering vs. flaming emissions from various biomass fuels: implications for health effects from wildland fires, Environmental health perspectives, 126, 017 011, 2018.

590 Knote, C., Hodzic, A., Jimenez, J., Volkamer, R., Orlando, J., Baidar, S., Brioude, J., Fast, J., Gentner, D., Goldstein, A., et al.: Simulation of semi-explicit mechanisms of SOA formation from glyoxal in aerosol in a 3-D model, Atmospheric Chemistry and Physics, 14, 6213–6239, 2014.

Koelemeijer, R., Homan, C., and Matthijsen, J.: Comparison of spatial and temporal variations of aerosol optical thickness and particulate matter over Europe, Atmospheric Environment, 40, 5304–5315, 2006.

595 Lang, M. N., Gohm, A., and Wagner, J. S.: The impact of embedded valleys on daytime pollution transport over a mountain range, Atmospheric Chemistry and Physics, 15, 11 981–11 998, 2015.

Lee, H., Liu, Y., Coull, B., Schwartz, J., and Koutrakis, P.: A novel calibration approach of MODIS AOD data to predict PM 2.5 concentrations, Atmospheric Chemistry and Physics, 11, 7991–8002, 2011.

Li, F., Zhang, X., and Kondragunta, S.: Highly anomalous fire emissions from the 2019–2020 Australian bushfires, Environmental Research
600 Communications, 3, 105 005, 2021.

Li, J., Han, Z., and Zhang, R.: Influence of aerosol hygroscopic growth parameterization on aerosol optical depth and direct radiative forcing over East Asia, Atmospheric research, 140, 14–27, 2014.

Liu, N., Zou, B., Feng, H., Tang, Y., and Liang, Y.: Evaluation and comparison of MAIAC, DT and DB aerosol products over China, Atmos. Chem. Phys. Discuss, pp. 1–34, 2019.

605 Liu, Y., Austin, E., Xiang, J., Gould, T., Larson, T., and Seto, E.: Health impact assessment of the 2020 Washington state wildfire smoke episode: excess health burden attributable to increased PM2. 5 exposures and potential exposure reductions, Geohealth, 5, e2020GH000 359, 2021.

Lv, B., Hu, Y., Chang, H. H., Russell, A. G., and Bai, Y.: Improving the accuracy of daily PM2. 5 distributions derived from the fusion of ground-level measurements with aerosol optical depth observations, a case study in North China, Environmental science & technology,
610 50, 4752–4759, 2016.

Lv, B., Hu, Y., Chang, H. H., Russell, A. G., Cai, J., Xu, B., and Bai, Y.: Daily estimation of ground-level PM2. 5 concentrations at 4 km resolution over Beijing-Tianjin-Hebei by fusing MODIS AOD and ground observations, Science of the Total Environment, 580, 235–244, 2017.

Lyapustin, A., Wang, Y., Korkin, S., and Huang, D.: MODIS collection 6 MAIAC algorithm, Atmospheric Measurement Techniques, 11,
615 5741–5765, 2018.

Ma, Z., Hu, X., Huang, L., Bi, J., and Liu, Y.: Estimating ground-level PM2. 5 in China using satellite remote sensing, Environmental science & technology, 48, 7436–7444, 2014.

Ma, Z., Liu, Y., Zhao, Q., Liu, M., Zhou, Y., and Bi, J.: Satellite-derived high resolution PM2. 5 concentrations in Yangtze River Delta Region of China using improved linear mixed effects model, Atmospheric Environment, 133, 156–164, 2016.

620 Martins, V. S., Lyapustin, A., de Carvalho, L. A., Barbosa, C. C. F., and Novo, E. M. L. d. M.: Validation of high-resolution MAIAC aerosol product over South America, Journal of Geophysical Research: Atmospheres, 122, 7537–7559, 2017.

Miller, D. J., Sun, K., Zondlo, M. A., Kanter, D., Dubovik, O., Welton, E. J., Winker, D. M., and Ginoux, P.: Assessing boreal forest fire smoke aerosol impacts on US air quality: A case study using multiple data sets, Journal of Geophysical Research: Atmospheres, 116, 2011.

625 Mills, M. J., Schmidt, A., Easter, R., Solomon, S., Kinnison, D. E., Ghan, S. J., Neely III, R. R., Marsh, D. R., Conley, A., Bardeen, C. G., et al.: Global volcanic aerosol properties derived from emissions, 1990–2014, using CESM1 (WACCM), Journal of Geophysical Research: Atmospheres, 121, 2332–2348, 2016.

Morrison, H. and Pinto, J.: Mesoscale modeling of springtime Arctic mixed-phase stratiform clouds using a new two-moment bulk microphysics scheme, Journal of the atmospheric sciences, 62, 3683–3704, 2005.

630 Morrison, H., Curry, J., and Khvorostyanov, V.: A new double-moment microphysics parameterization for application in cloud and climate models. Part I: Description, Journal of the atmospheric sciences, 62, 1665–1677, 2005.

Neumann, J. E., Amend, M., Anenberg, S., Kinney, P. L., Sarofim, M., Martinich, J., Lukens, J., Xu, J.-W., and Roman, H.: Estimating PM2. 5-related premature mortality and morbidity associated with future wildfire emissions in the western US, Environmental Research Letters, 16, 035 019, 2021.

635 O'Dell, K., Ford, B., Fischer, E. V., and Pierce, J. R.: Contribution of wildland-fire smoke to US PM2. 5 and its influence on recent trends, Environmental science & technology, 53, 1797–1804, 2019.

Powers, J. G., Klemp, J. B., Skamarock, W. C., Davis, C. A., Dudhia, J., Gill, D. O., Coen, J. L., Gochis, D. J., Ahmadov, R., Peckham, S. E., et al.: The weather research and forecasting model: Overview, system efforts, and future directions, Bulletin of the American Meteorological Society, 98, 1717–1737, 2017.

640 Qin, W., Fang, H., Wang, L., Wei, J., Zhang, M., Su, X., Bilal, M., and Liang, X.: MODIS high-resolution MAIAC aerosol product: Global validation and analysis, Atmospheric Environment, 264, 118 684, 2021.

Reid, J., Koppmann, R., Eck, T., and Eleuterio, D.: A review of biomass burning emissions part II: intensive physical properties of biomass burning particles, Atmospheric chemistry and physics, 5, 799–825, 2005.

Sayeed, A., Lin, P., Gupta, P., Tran, N. N. M., Buchard, V., and Christopher, S.: Hourly and Daily PM2. 5 Estimations Using MERRA-2: A
645 Machine Learning Approach, Earth and Space Science, 9, e2022EA002 375, 2022.

Schroeder, W., Oliva, P., Giglio, L., and Csiszar, I. A.: The New VIIRS 375 m active fire detection data product: Algorithm description and initial assessment, Remote Sensing of Environment, 143, 85–96, 2014.

Singh, M. K., Venkatachalam, P., Gautam, R., et al.: Geostatistical methods for filling gaps in Level-3 monthly-mean aerosol optical depth data from multi-angle imaging spectroradiometer, Aerosol and Air Quality Research, 17, 1963–1974, 2017.

650 Skamarock, W. C., Klemp, J. B., Dudhia, J., Gill, D. O., Liu, Z., Berner, J., Wang, W., Powers, J. G., Duda, M. G., Barker, D. M., et al.: A description of the advanced research WRF model version 4, National Center for Atmospheric Research: Boulder, CO, USA, 145, 145, 2019.

Soares, J., Sofiev, M., and Hakkarainen, J.: Uncertainties of wild-land fires emission in AQMEII phase 2 case study, Atmospheric Environment, 115, 361–370, 2015.

655 Solomos, S., Amiridis, V., Zanis, P., Gerasopoulos, E., Sofiou, F., Herekakis, T., Brioude, J., Stohl, A., Kahn, R., and Kontoes, C.: Smoke dispersion modeling over complex terrain using high resolution meteorological data and satellite observations–The FireHub platform, Atmospheric Environment, 119, 348–361, 2015.

Song, W., Jia, H., Huang, J., and Zhang, Y.: A satellite-based geographically weighted regression model for regional PM2. 5 estimation over the Pearl River Delta region in China, Remote Sensing of Environment, 154, 1–7, 2014.

660 Sun, H., Jiao, R., Xu, H., An, G., and Wang, D.: The influence of particle size and concentration combined with pH on coagulation mechanisms, Journal of Environmental Sciences, 82, 39–46, 2019.

Val Martin, M., Kahn, R. A., and Tosca, M. G.: A global analysis of wildfire smoke injection heights derived from space-based multi-angle imaging, Remote Sensing, 10, 1609, 2018.

Wang, J. and Christopher, S. A.: Intercomparison between satellite-derived aerosol optical thickness and PM2. 5 mass: Implications for air

665 quality studies, Geophysical research letters, 30, 2003.

Wegesser, T. C., Pinkerton, K. E., and Last, J. A.: California wildfires of 2008: coarse and fine particulate matter toxicity, Environmental health perspectives, 117, 893–897, 2009.

Wei, J., Huang, W., Li, Z., Xue, W., Peng, Y., Sun, L., and Cribb, M.: Estimating 1-km-resolution PM2. 5 concentrations across China using the space-time random forest approach, Remote Sensing of Environment, 231, 111 221, 2019.

670 Wiedinmyer, C., Akagi, S., Yokelson, R. J., Emmons, L., Al-Saadi, J., Orlando, J., and Soja, A.: The Fire INventory from NCAR (FINN): A high resolution global model to estimate the emissions from open burning, Geoscientific Model Development, 4, 625–641, 2011.

Wu, Y., Arapi, A., Huang, J., Gross, B., and Moshary, F.: Intra-continental wildfire smoke transport and impact on local air quality observed by ground-based and satellite remote sensing in New York City, Atmospheric Environment, 187, 266–281, 2018.

Xiao, Q., Wang, Y., Chang, H. H., Meng, X., Geng, G., Lyapustin, A., and Liu, Y.: Full-coverage high-resolution daily PM2. 5 estimation

675 using MAIAC AOD in the Yangtze River Delta of China, Remote Sensing of Environment, 199, 437–446, 2017.

Xiao, Q., Geng, G., Cheng, J., Liang, F., Li, R., Meng, X., Xue, T., Huang, X., Kan, H., Zhang, Q., et al.: Evaluation of gap-filling approaches in satellite-based daily PM2. 5 prediction models, Atmospheric Environment, 244, 117 921, 2021.

Xie, Y., Wang, Y., Zhang, K., Dong, W., Lv, B., and Bai, Y.: Daily estimation of ground-level PM2. 5 concentrations over Beijing using 3 km resolution MODIS AOD, Environmental science & technology, 49, 12 280–12 288, 2015.

680 Xue, T., Zheng, Y., Tong, D., Zheng, B., Li, X., Zhu, T., and Zhang, Q.: Spatiotemporal continuous estimates of PM2. 5 concentrations in China, 2000–2016: A machine learning method with inputs from satellites, chemical transport model, and ground observations, Environment international, 123, 345–357, 2019.

Xue, Z., Gupta, P., and Christopher, S.: Satellite-based estimation of the impacts of summertime wildfires on PM 2.5 concentration in the United States, Atmospheric Chemistry and Physics, 21, 11 243–11 256, 2021.

685 Yang, Z., Demoz, B., Delgado, R., Sullivan, J., Tangborn, A., and Lee, P.: Influence of the transported Canadian wildfire smoke on the ozone and particle pollution over the Mid-Atlantic United States, Atmospheric Environment, 273, 118 940, 2022.

Zamani Joharestani, M., Cao, C., Ni, X., Bashir, B., and Talebiesfandarani, S.: PM2. 5 prediction based on random forest, XGBoost, and deep learning using multisource remote sensing data, Atmosphere, 10, 373, 2019.

Zandi, S., Ghobakhlou, A., and Sallis, P.: Evaluation of spatial interpolation techniques for mapping soil pH, 2011.

690   Zaveri, R. A., Easter, R. C., Fast, J. D., and Peters, L. K.: Model for simulating aerosol interactions and chemistry (MOSAIC), Journal of
        Geophysical Research: Atmospheres, 113, 2008.

        Zhang, G., Rui, X., and Fan, Y.: Critical review of methods to estimate PM2. 5 concentrations within specified research region, ISPRS
        International Journal of Geo-Information, 7, 368, 2018.

        Zhou, S., Collier, S., Jaffe, D. A., Briggs, N. L., Hee, J., Sedlacek III, A. J., Kleinman, L., Onasch, T. B., and Zhang, Q.: Regional influence

695   of wildfires on aerosol chemistry in the western US and insights into atmospheric aging of biomass burning organic aerosol, Atmospheric
        Chemistry and Physics, 17, 2477–2493, 2017.

        Zimmerman, N., Presto, A. A., Kumar, S. P., Gu, J., Hauryliuk, A., Robinson, E. S., Robinson, A. L., and Subramanian, R.: A machine
        learning calibration model using random forests to improve sensor performance for lower-cost air quality monitoring, Atmospheric Mea-
        surement Techniques, 11, 291–313, 2018.
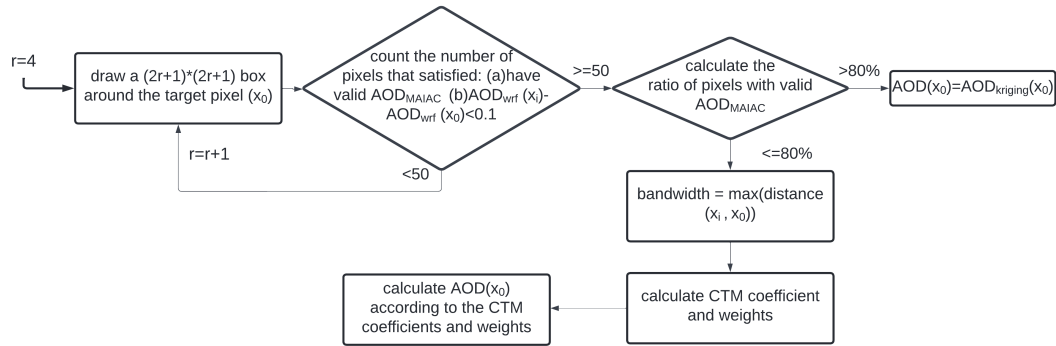
Fig. 1. *flowchart of the AOD gap-filling process. "r" referse to the radius of the selected box used in the process.*
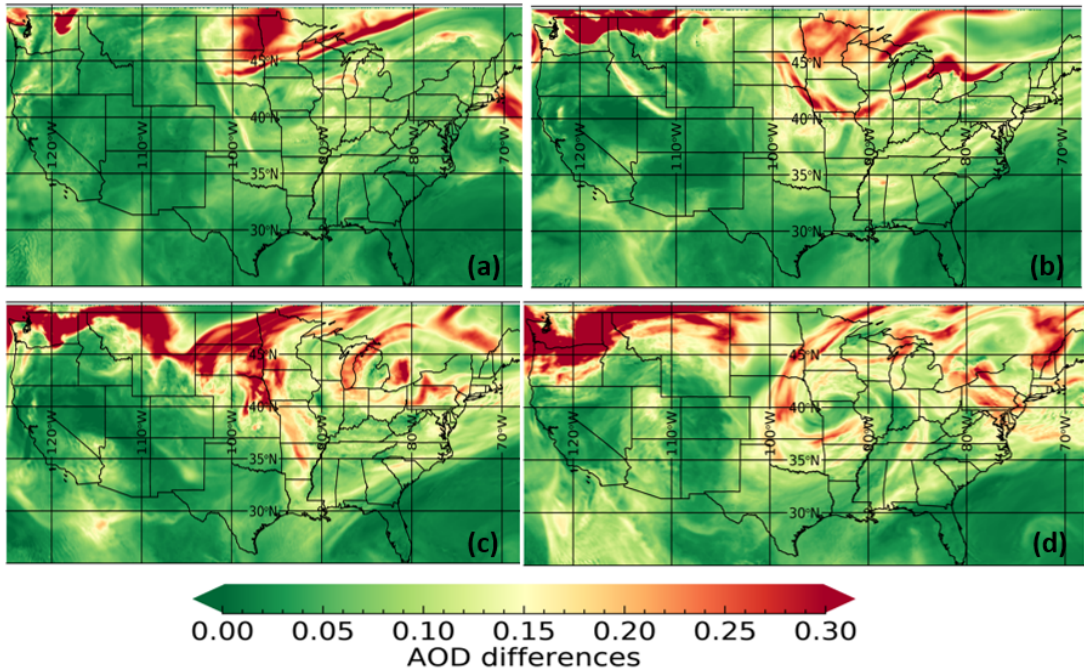
Fig. 2. *AOD change due to Canadian wildfires from August 17th to 20th, 2018: (a)August 17th,2018; (b)August 18th,2018; (c)August 19th,2018; (d) August 20th,2018. The AOD change is calculated using the difference of two WRF-Chem simulations.*
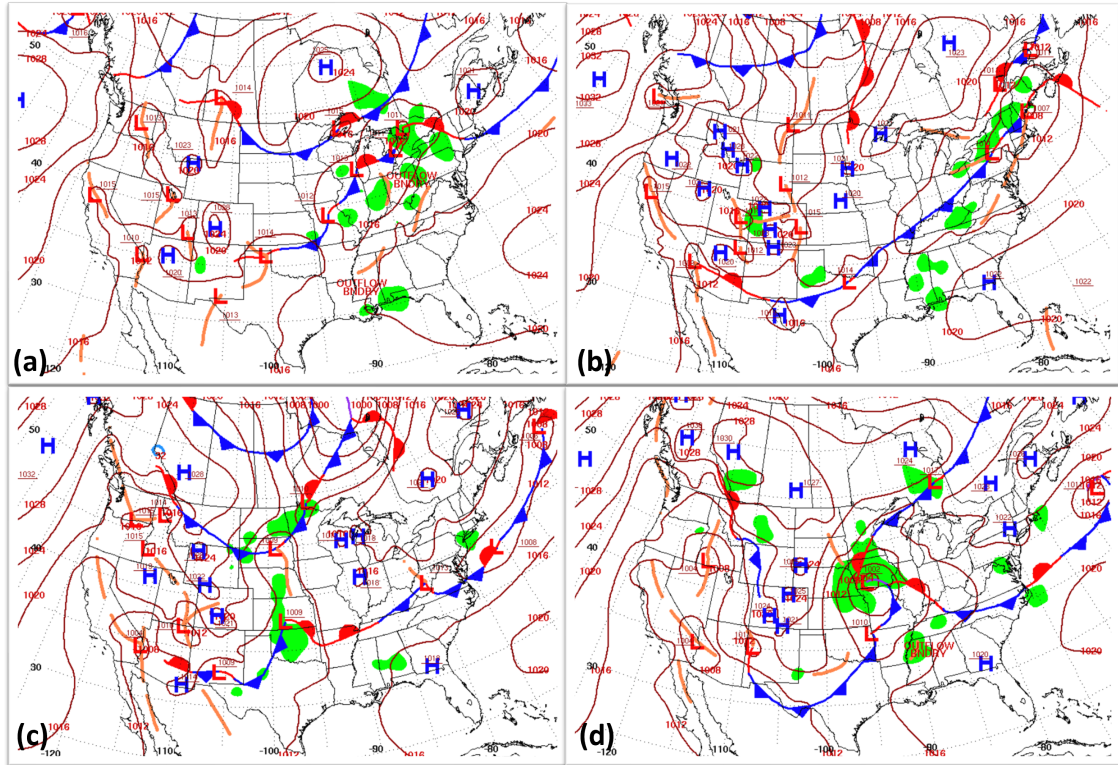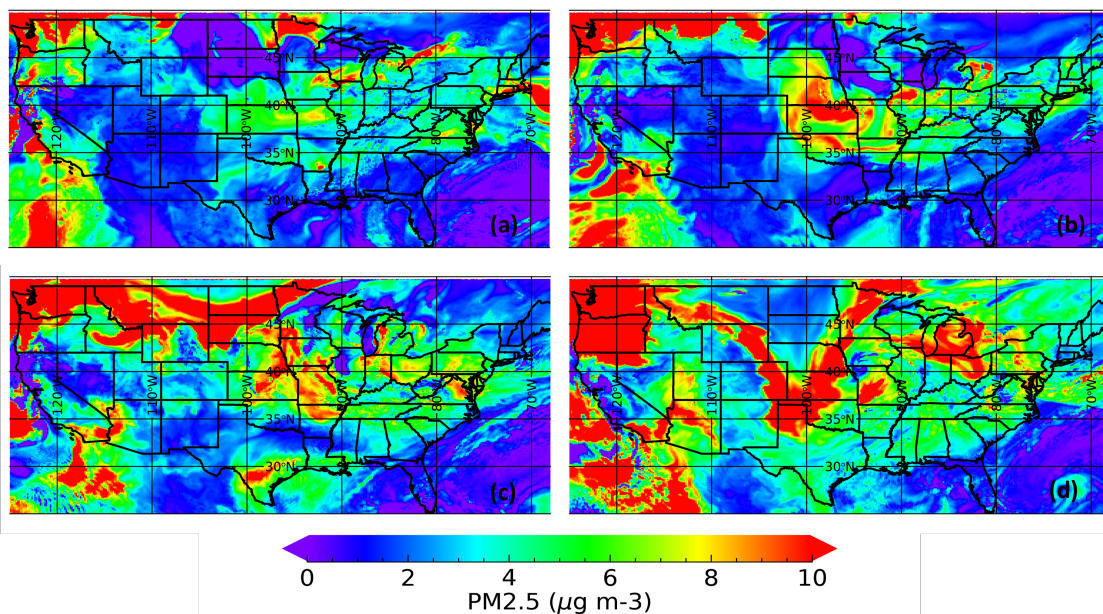
Fig. 3. *Surface weather maps from August 17th to 20th, 2018 (https://www.wpc.ncep.noaa.gov/archives/web_pages/sfc/sfc_archive.php): (a)August 17th,2018; (b)August 18th,2018; (c)August 19th,2018; (d) August 20th,2018.*

26
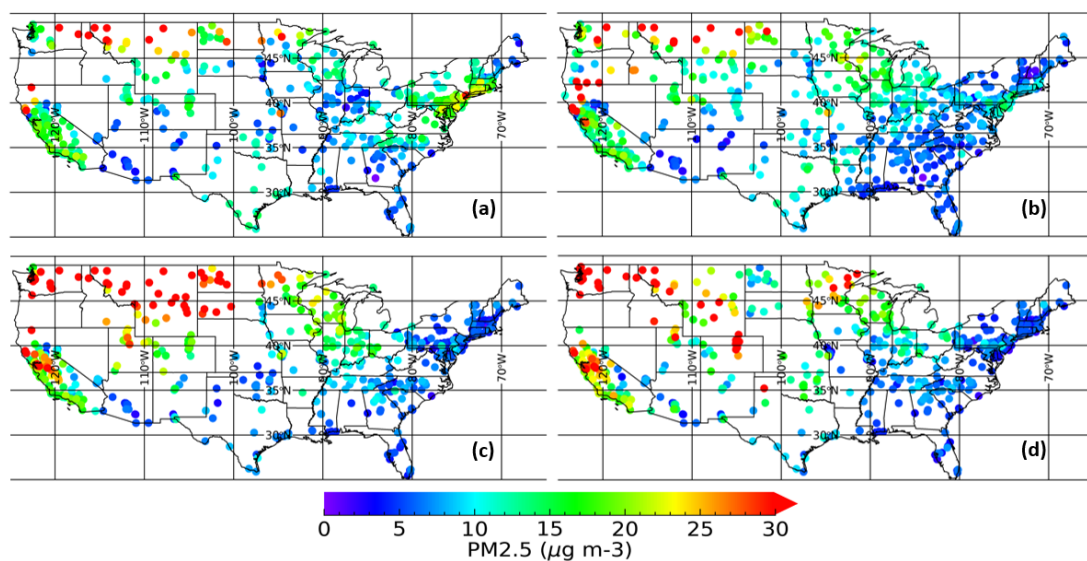
Fig. 4. *Surface PM2.5 measurements from EPA stations over CONUS from August 17th to 20th, 2018: (a)August 17th,2018; (b)August 18th,2018; (c)August 19th,2018; (d) August 20th,2018.*

Fig. 5. *Surface PM2.5 dry mass difference from WRF-Chem simulation over CONUS from August 17th to 20th, 2018: (a)August 17th,2018; (b)August 18th,2018; (c)August 19th,2018; (d) August 20th,2018. The PM2.5 difference is calculated using the two WR-Chem simulations.*
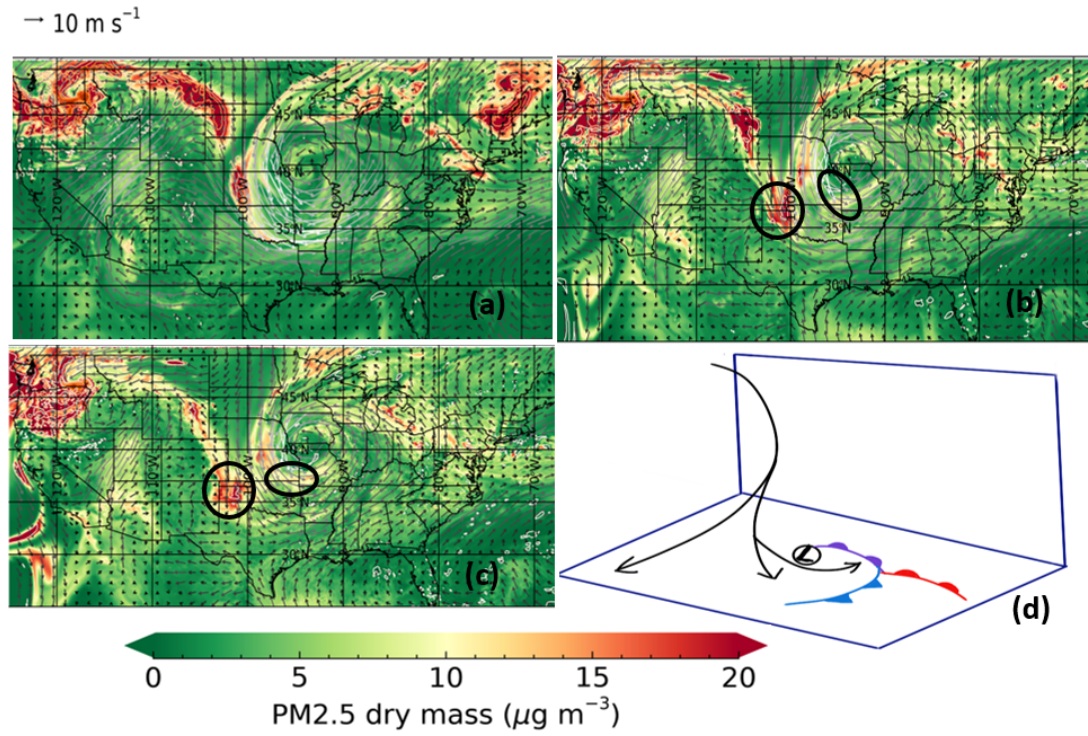
Fig. 6. *PM2.5 dry mass distribution on August 20th,2018 at different levels (a)773hPa (b)850hPa (c)900hPa (d)conceptual model of airflow patterns in a typical extratropical cyclone based on (Cotton et al., 2011).*
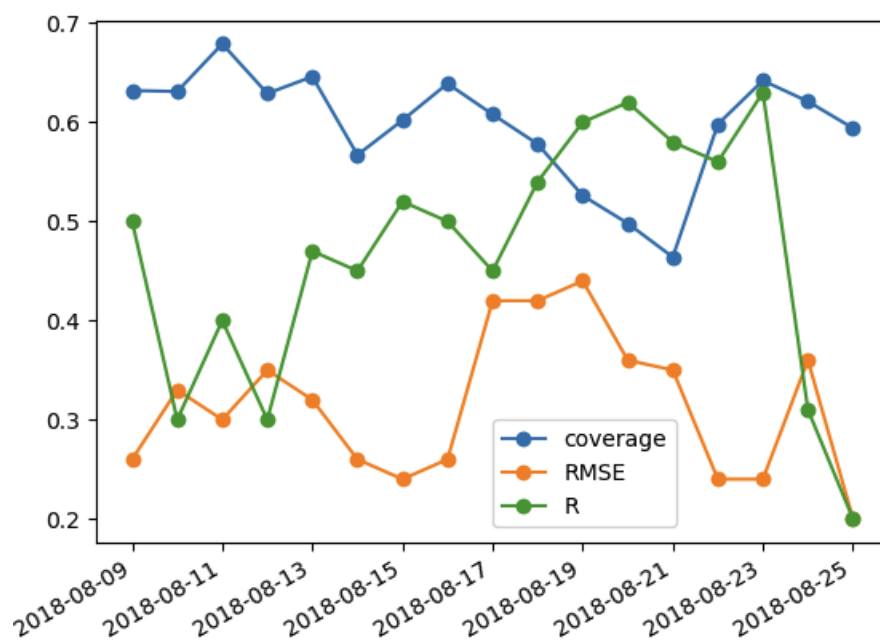
Fig. 7. *Time seires of MAIAC AOD coverage (blue line), correlation coefficient (green line) and RMSE (orange line) of two AOD products (WRF-CHEM AOD and MAIAC AOD).*
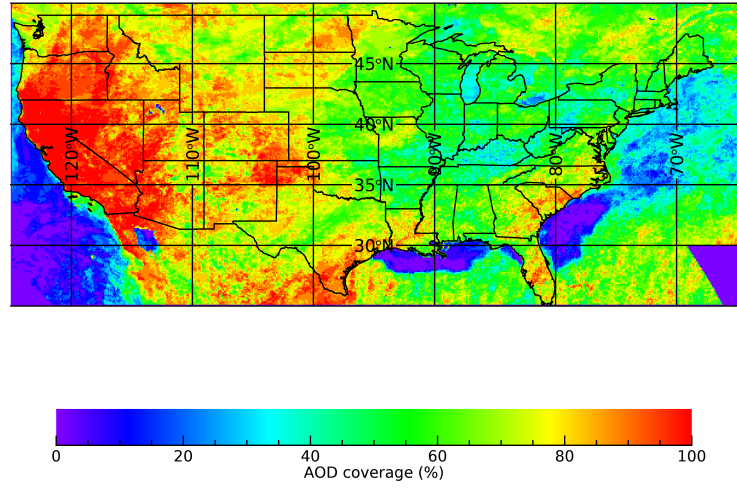
Fig. 8. *AOD coverage during the 17-day period*
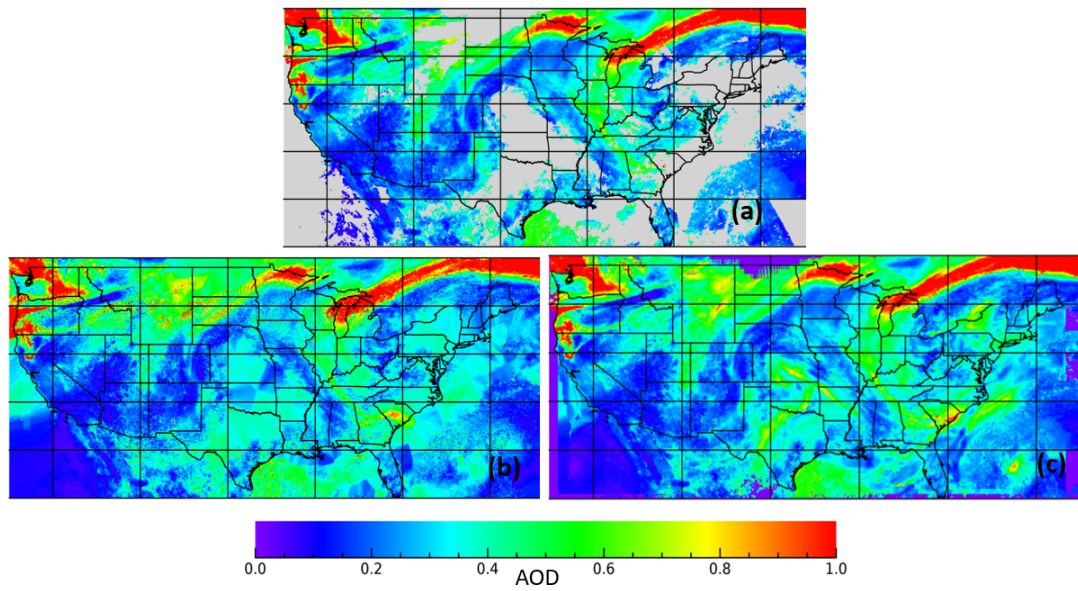
Fig. 9. *AOD distribution from (a) MAIAC, (b) Kriging method and (c)CTM-filled AOD on August 13th 2018.*
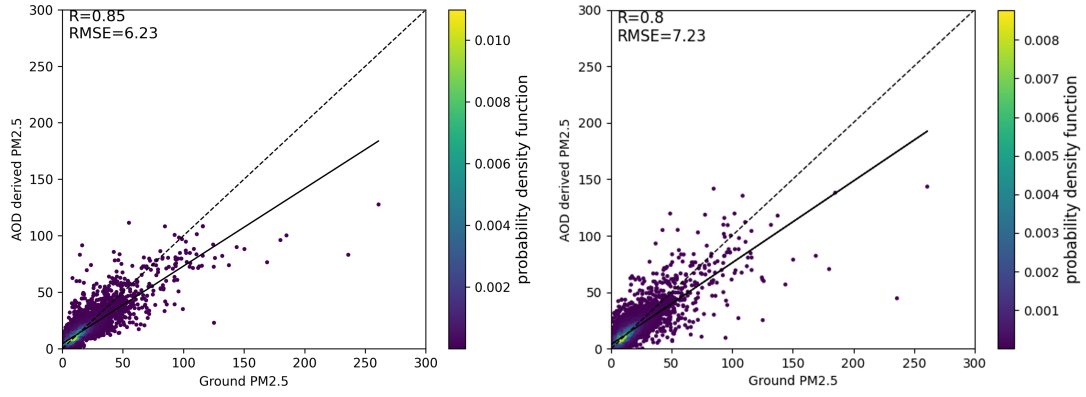
Fig. 10. *Fitting and 100-fold cross validation results for GWR method*
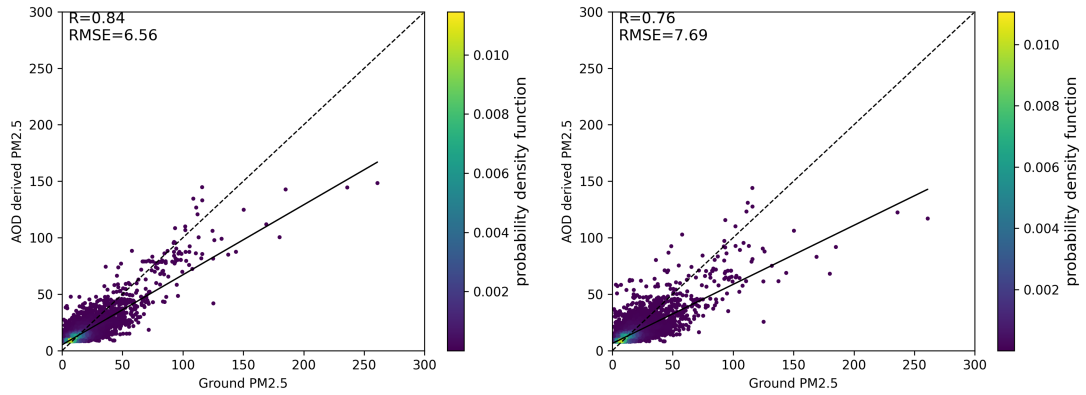
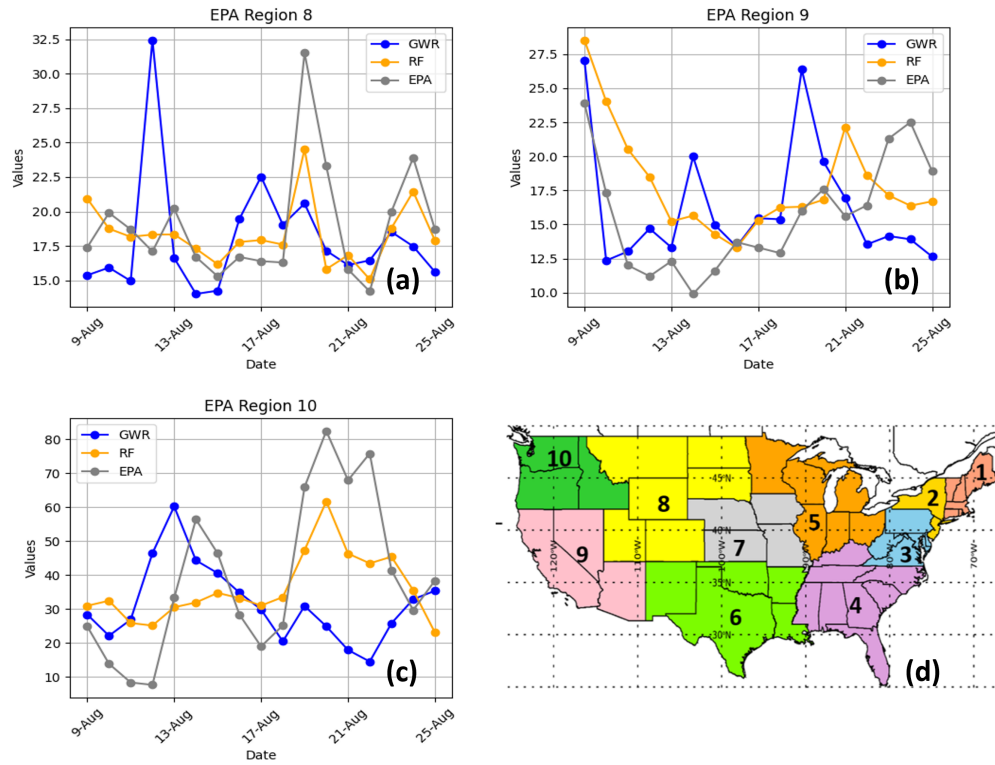**Fig. 11.** *Fitting and 100-fold cross validation results for RF method*

Fig. 12. *Mean PM2.5 concentration variations over the top 3 polluted areas (a) EPA region 8 (b) EPA region 9 (c) EPA region 10 (d)EPA region map*